Materials Research Bulletin 97 (2018) 71–80

Contents lists available at ScienceDirect

Materials Research Bulletin

journal homepage: www.elsevier.com/locate/matresbu

Structure, morphology and photoluminescence attributes of Al/Ga co-doped ZnO nanofilms: Role of annealing time

Hayder J. Al-Asedy[a,b,c], Noriah Bidin[a,*], Khaldoon N. Abbas[a,b,d], Mohammed A. Al-Azawi[a,b]

[a] University Technology Malaysia, Laser Center, Ibnu Sina Institute for Scientific and Industrial Research, Johor Bahru, Johor, 81310, Malaysia
[b] Universiti Teknologi Malaysia, Department of Physics, Faculty of Science, Johor Bahru, Johor, 81310, Malaysia
[c] Al-Qadisiyah University, Faculty of Education, Physics Department, Diwaniya 00964, Iraq
[d] Al-Mustansiriya University, Faculty of Science, Physics Department, Baghdad 00964, Iraq

ARTICLE INFO

Keywords:
Particle- and flake-like AGZO nanofilms
Annealing time
Morphology
Structure
Photoluminescence
Raman spectra

ABSTRACT

The influence of annealing time on the structure, morphology and photoluminescence behavior (Al)/(Ga) co-doped ZnO (AGZO). nanofilms are grown on the p-type Si(100) substrate via combined sol-gel, spin coating annealed in air at 500 °C at 0–3 h. Samples are characterized using XRD, TEM, AFM, FESEM, EDX, (PL) and Raman measurements. XRD pattern confirmed the growth of highly poly-crystalline hexagonal wurtzite structure of ZnO with preferred orientation along (101) direction. At (3 h) is found to cause lattice contraction and strain relaxation. TEM images revealed the nucleation of nanoparticles (NPs) and SAED pattern identified the lattice parameter. Raman spectra of AGZO exhibited optical and acoustic modes. FESEM displayed an increase in the particles size and number of nanoflakes with increasing annealing time. EDX detected right elemental traces. PL revealed an intense emission peak centered at 3.23 eV, which is continuously shifted toward lower frequency with increasing time.

1. Introduction

In the past few decades, tremendous progress is made towards the synthesis and characterization of semiconducting oxides in general and ZnO in particular due to their unprecedented prospect for optoelectronic devices, sensors, and other technological applications [1]. ZnO is a well-known wide band gap (3.37 eV) semiconductor and piezoelectric material with large exciton binding energy (60 meV) at room temperature [2], [3]. Besides, it finds diverse applications as catalysts, sensors, piezoelectric transducers [4], transparent conductors [5] and surface acoustic wave devices [6]. Over the years, several techniques are developed to prepare the ZnO thin films including thermal oxidation [7], molecular beam epitaxy [8] and pulsed laser deposition [9], chemical vapour deposition [10] and magnetron sputtering [11] etc. to cite a few. Amongst all these, sol-gel [12–15] method has some merits, such as the easy control of chemical components, and fabrication of thin film at a low cost (cost effective process), excellent control of the stoichiometry, composition modification (mixing on a molecular level), inexpensive equipments and the sol–gel technology is a facile technological approach offering possibility for production of high quality homogeneous thin films on large area [16], followed by spin coating became attractive for ZnO nanofilm fabrication due to its high controllability on nanostructure properties mediated by flexible growth conditions. Recently, investigation of metallic elements doped/co-doped ZnO nanofilm received much attention due to some emerging properties as compared to their pure counterparts.

Many researches revealed that the overall electronic properties of grown nanostructure are greatly decided by the deposition conditions and post-annealing treatment. Generally, the properties of the as-deposited films are strongly sensitive to the presence of structural defects which are requisite for thin films growth for maintaining the stabile properties after the post-annealing treatment. Such post-annealing is performed to alter the stoichiometry, carrier concentration, and mobility. In addition, it is used to improve the film crystallinity as well as the physical desorption or the chemisorption of oxygen from the grain boundaries of films. In short, the overall properties of ZnO films are determined not only by the growth processes but also by the post growth treatment such as thermal annealing. Earlier, extensive researches are carried out to evaluate the effects of annealing on the properties of ZnO thin films [17–19]. Despite much research, no conclusive remark is made regarding the influence of the annealing conditions on the properties of ZnO thin films such as ambient gas species, annealing temperature and time. Especially, the effects of annealing time on the structural and optoelectronic properties of Al/Ga doped

* Corresponding author.
E-mail addresses: hayder_jawaad@yahoo.com (H.J. Al-Asedy), noriah@utm.my (N. Bidin).

http://dx.doi.org/10.1016/j.materresbull.2017.08.050
Received 22 December 2016; Received in revised form 23 August 2017; Accepted 26 August 2017
Available online 30 August 2017
0025-5408/

ZnO films are not much explored.

Single element doped ZnO thin films such as Al:ZnO (AZO) and Ga:ZnO (GZO) suffer from various limitations in terms of thermal stability, distortion in the crystal structures as well as easy oxidation [20]. For instance, the distortion in GZO crystal structure is less than AZO because of the lower approximate ionic radii of Ga^{3+} (0.062 nm) to Zn^{2+} (0.074 nm) than Al^{3+} (0.054 nm) [21]. Conversely, less durabiity of GZO under humid conditions and expensiveness of Ga inhibit their mass production. ZnO co-doping mechanism can improve the electrical and optical properties with doping process such as Al and Ga elements which are belong to III group, exciton and charge carriers transport in organic layer need to be a short distance between organic film and transparent conducting oxide layer less than 10 nm. To satisfy this requirement, the transparent conducting oxide should be nanoscale in dimensions. Therefore, nanostructured transparent conducting oxide can enhance the performance of nanostructure films application with increasing charge collection area. Co-doping of ZnO is normally performed using physical methods [22]. However, for achieving good homogeneity and increased formation of transparent conductive oxides sol-gel method of synthesis is preferred.

By considering the notable advantages of combined sol-gel and spin coating method we prepare Al/Ga co-doped ZnO thin films (AGZO) on p-type Si (100) substrate under varying annealing time. Annealing time dependent structural, morphological and photoluminescence properties of these as-prepared nanofilm samples are determined. Results are analyzed, compared and explained using different mechanisms.

2. Experimental

Sol–gel and spin coating methods are used to deposit AGZO nanofilms onto p-type Si (100) substrates. Analytical grade high purity raw materials are taken for sample preparation, where zinc precursor solution is obtained by dissolving zinc acetate dihydrate (ZnAc) [$Zn(CH_3COO)_2{\cdot}2H_2O$] (Alfa Aesar, 99.999%) in 2-propanol (C_3H_8O) of 0.1 M concentration, and ethanolamine (EA) (AR, Merck). Next, EA is added to get a transparent and stable solution where (ZnAc), 2-propanol and EA are used and solvent and stabilizer, respectively. The molar ratios of ZnAc to EA are maintained at 1:1. Aluminum nitrate nonahydrate [$Al(NO_3)_3{\cdot}9H_2O$] as well as gallium nitrate nonahydrate [$Ga(NO_3)_3{\cdot}9H_2O$] (Alfa Aesar, 99.999%) are used as Al and Ga doping resources, respectively. Concentrations of both Al and Ga are fixed to 1 at.%. Aluminum nitrate nonahydrate and gallium nitrate nonahydrate are dissolved into the solution, which is stirred using magnetic stirrer at 60 °C for 90 min.

A transparent and homogenous solution that appeared after 24 h is then spin coated onto Si substrates. The entire procedure of coating and drying is performed for 30 s at 3000 rpm. After the deposition, the films are dried in a furnace (300 °C) for 10 min. The baked films revealed the absence of vibration peaks (FTIR spectra) at 1580 and 1450–1420 cm^{-1} corresponding to the acetate group [23]. Moreover, the absence of these peaks verified the complete removal of organic constituents at 300 °C which is considered as the optimal temperature to induce the growth of nanocrystallites on the spin-coated AZO film [24]. The coating to drying process is repeated for 10 times. The achieved AGZO nanostructured films are annealed in microprocessor controlled furnace (500 °C) at heating rate of 5 °C/min for the duration of 0, 1.0, 2.0, and 3.0 h.

The morphology and structure of (all) synthesized samples are characterized using atomic force microscopy (AFM, SPI3800, Seiko Instrument Inc.), X-ray diffraction (XRD, Bruker D8 Advance Diffractometer) operated with Cu-Kα_1 radiations (1.5406 A°) at 40 kV and 100 mA in the scanning range (2θ) of 20°–80°. A slow speed of scanning ~1.2°/min with a resolution of 0.01° is employed. Samples elemental composition and surface morphology are analyzed using energy dispersive X-ray diffractometer (EDX) and field emission scanning electron microscope (FESEM, ZEISS SUPRA 35 VP), respectively.

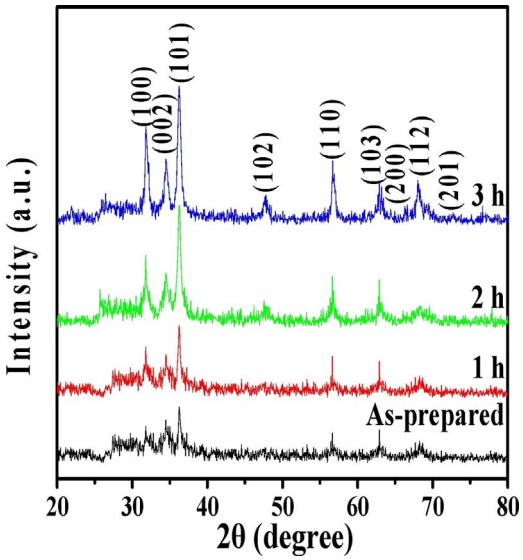

Fig. 1. XRD pattern of as grown and post annealed samples.

Transmission electron microscope (TEM) micrographs and selected-area electron diffraction patterns were obtained by (Hitachi) model HT7700, and high-resolution transmission electron microscope (HRTEM) (JEOL JEM-ARM200F). Room temperature photoluminescence (PL) measurement is performed using as Perkin Elmer LS 55 Luminescence Spectrometer, where xenon flash lamp with exciton 320 nm is used as excitation source. Raman spectra of the films were obtained by means of labRam HR Evolution (RAMAN SPECTROMETER) Brand: HORIBA Scientific. Raman spectra were excited with the 325 nm line at Ultra-Violet and He-Cd laser at an incident power of 20 mW in the range 1800–2400 grating/mm. The resistivity of the annealed (at 500 °C) AGZO nanofilms is measured using four-point probe method.

3. Results and discussion

Fig. 1 shows the XRD pattern of pre-annealed and post-annealed AGZO nanofilms samples. The appearance of sharp diffraction peaks clearly reveals the existence of high crystalline nature of the samples [25]. Peaks corresponding to the growth directions (lattice planes) of (100), (002), (101), (102), (110), (103), (200), (112) and (201) are evidenced in all samples. All the samples exhibit hexagonal wurtzite polycrystalline structure when compared with the standard JCPDS of ZnO (Card no. 36-1451) [25]. Our AGZO nanofilms with 1 at.% Al and additional 1 at.% Ga co-doping did not display the formation of secondary phases or impurities such as Al_2O_3, Ga_2O_3, $ZnAl_2O_4$ or $ZnGa_2O_4$. Moreover, the observed enhancement in the XRD intensity for (100), (002) and (101) peaks of all samples indicates the preferential growth orientation along these lattice planes. A decrease in the full width at half maxima (FWHM) of these peaks with increasing annealing time shows the role of size confinement. Scherrer equation is used to estimate the grain size (D) of Nano crystallites by fitting the peak to Gaussian profile [26]. The grain sizes are increased with the increase of annealing time duration from 1 to 3 h, thereby caused enhanced crystallinity of the nanofilms. Thus, an improvement in the crystalline nature of the films is achieved by controlling the annealing time. This annealing time assisted modification in the nanofilms growth is attributed to rapid reduction of the number of non-bridging oxygen type defects and subsequent favourable formation of the ZnO grains.

The dislocation density (δ) being defined as the length of the dislocation lines per unit volume of crystal, exhibits a decreasing trend with increasing annealing time. Consequently, the concentration of lattice imperfections is decreased. The dislocation density in the film is determined using Williamson and Smallman's formula ($\delta = 1/D^2$) [27]

Table 1
Annealing time dependent variation of growth orientation, diffraction angle, planer separation, lattice parameters, and dislocation density.

Annealing time (h)	*hkl*	2θ ± 0.01	d_{hkl} (nm) ± 0.0002	Lattice parameter (nm) ± 0.0002	δ ± 0.0002
As-prepared	(100)	31.76	0.2829	a = 0.3256	0.0156
	(002)	34.46	0.2602	c = 0.5209	
	(101)	36.38	0.2594		
1	(100)	31.77	0.2825	a = 0.3250	0.0082
	(002)	34.49	0.2598	c = 0.5206	
	(101)	36.38	0.2581		
2	(100)	31.78	0.2817	a = 0.3248	0.0020
	(002)	34.47	0.2594	c = 0.5202	
	(101)	36.38	0.2563		
3	(100)	31.75	0.2813	a = 0.3245	0.0011
	(002)	34.48	0.2584	c = 0.5198	
	(101)	36.38	0.2358		

and enlisted in Table 1. The larger *D* and smaller FWHM values indicate better crystallization of the ZnO nanostructured thin films. The expressions for lattice parameters (*a* and *c*) yield [28]:

$$D = \frac{K\lambda}{\beta \cos\theta_{101}} \quad (1)$$

$$a = \frac{\lambda}{\sqrt{3} \sin\theta_{100}} \quad (2)$$

$$c = \frac{\lambda}{\sin\theta_{002}} \quad (3)$$

Considerable shift in the (101) peak position towards higher diffraction angle (Table 1) with increasing annealing time indicated the change in the lattice parameter due to the involvement of macroscopic strain. This decrease in the lattice parameters is attributed to various mechanisms including the elimination of defects and occurrence of structural relaxation. ZnO thin films having various defects such as oxygen vacancies, lattice disorders, etc are very sensitive to the annealing process, where removal of these defects can cause considerable amount of lattice contraction.

Table 2 summarizes the annealing temperature dependent variation of estimated grain size using different methods, values of resistivity as well as density (Eq. (4)). As-prepared sample (0 h) revealed a grain size of 9 nm, which is grown to as much as 13, 22 and 30 nm after 1, 2 and 3 h of annealing time; respectively. The average grain size of as-deposited film is 15.1 nm. However, it is shown to increase from 25.3 to 36.3 nm with the increase of annealing time duration from 1 to 6 h for nanofiber thin films grown by spray pyrolysis technique [29]. This indicated an improvement in the crystalline nature of the film with increasing annealing time duration. The growth of granules with the increase of annealing time promoted the reduction of the number of non-bridging oxygen type defects which in turn favored the formation of the ZnO grains [30]. Meanwhile, an improvement in the overall crystallinity of AGZO films with increasing annealing time is also evidenced. Also we can notice by increased time the crystallite size is increasing, as shown in Fig. 2. Table 2 enlists the values of nanocrystallites density (ρ) and cell volume (V) for hexagonal crystal system in terms of lattice

Table 2
Annealing time dependent variation of estimated grain size obtained using different methods, resistivity, and density.

Annealing time (h)	Grain size (nm)		FWHM	Resistivity (Ω cm)	Density (gm/cm^3)
	Scherrer	AFM			
As-prepared	09.00	08	0.01621	0.167	5.7197
1	13.00	16	0.01122	0.098	5.7442
2	23.12	25	0.00631	0.046	5.7557
3	30.03	35	0.00486	0.024	5.7708

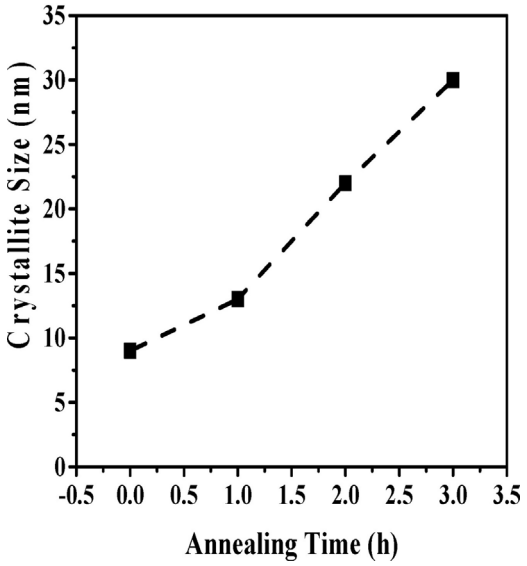

Fig. 2. Variation of nanocrystallite sizes as a function of annealing time.

constants *a* and c which are calculated from the XRD patterns following [31]:

$$\rho = \frac{1.6609 \times M \times n}{V} \quad (4)$$

$$V = 0.866\ a^2 \times c \quad (5)$$

Where M is molecular weight of substance and n is the number of formula units in the unit cell (n = 2 for ZnO).

The density of film is enhanced with increasing annealing time. This is due to the embodiment of nanostructures having less number of point defects, smaller d or higher D in the presence of highly crystalline ZnO nanoparticales, vacancies (cation and anion), extended defects like dislocations, etc. These defects are responsible changing the density and bulk modulus [31]. Therefore, for single element doping (Al only) the low concentration of Al^{3+} has neutralized these defects and do not influence the crystallize size. However, for co-doped system (Al and Ga dopants) the increased concentration of Al^{3+} and Ga^{3+} ions has increased the size where the strain became thickness dependent. The increase in the density with the increase in Al/Ga concentration produced a contraction in the lattice volume.

These defects allowed the alteration in the density and resistivity of the film. Furthermore, the annealing temperature assisted lattice relaxation due to varying dangling bonds played a significant role in modifying the overall film structures. The electrostatic interaction of the dangling bonds on ZnO surface with adsorbed oxygen ions from the atmosphere is partly responsible for the contraction of lattice (Table 1).

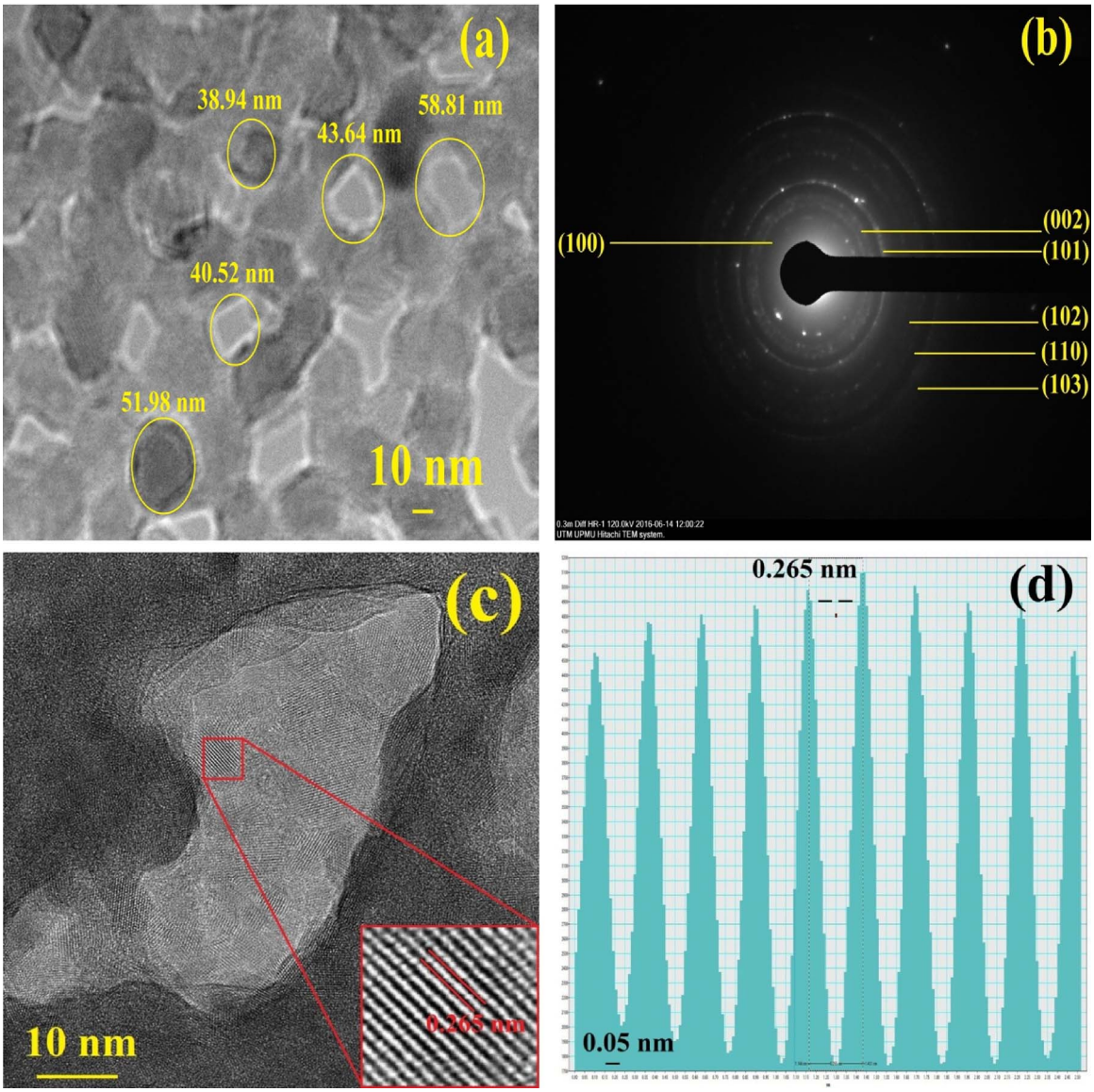

Fig. 3. (a) TEM image of AGZO films annealed for 3 h is showing the existence of NPs. (b) FFT image of selected NP showing various Bragg's plane with SAED pattern of a NP (inset). (c) HRTEM image. (d) profile of one view.

Fig. 3(a) displays the TEM images of the AGZO nanofilms annealed for 3 h, where the growth of crystalline NPs is clearly evidenced. Fig. 3(b) shows the FFT pattern from the selected part (20 nm) of Fig. 3(a). The Bragg's diffraction planes of the crystal lattice are observed. Occurrences of series of rings confirmed that these column structures are indeed AGZO with the (002) plane parallel to the Si substrate surface. The selected area electron diffraction (SAED) pattern of the film (Fig. 3(c)) clearly revealed the manifestation of AGZO lattice. The HRTEM image in Fig. 3(c) clearly resolved the lattice fringes with inter-plane distance of 0.265 nm, which is matched with the (002) for angle (34°) lattice plane of AGZO [32]. Furthermore, the formation of polycrystalline film with multilayer growth pattern consisting of NPs and nanoflakes revealed the presence of round-shaped crystallites with distinct crystallographic planes. Fig. 3(d) illustrates the single profile lattice fringes. This achieved high regularity in the fringe profile obtained via annealing process further confirmed the good quality, homogeneity and enhanced crystallinity of the nanostructure [32].

Fig. 4 depicts the annealing time dependent AFM images. The corresponding size distributions of nanocrystallites are shown in Fig. 5. The overall growth morphology of the AGZO nanofilm is observed to be highly sensitive to annealing[33]. The direct formation of grains on the substrate surface and their structural evolution with annealing time is attributed to the Volmer–Weber (VW) growth mechanism. In this process, the interactions between adatoms became stronger than those of the adatom with the surface, leading to the formation of three-dimensional adatom clusters or islands as observed in the AFM images. Eventually, the growth of these AGZO clusters (NPs and nanoflakes) together with coarsening resulted the formation of rough multi-layer films on the Si(100) substrate surface. The NSs are preferentially grown perpendicular to the substrate of double layered thin films. Xu et al. [34] proposed that the (002) plane of ZnO has minimum surface energy so most of the particles grow along this plane. However, as the number of layer increases with increasing annealing time duration, the layers beneath act as buffer layer for the top layers. AFM images of the ZnO thin film (Fig. 4(a), (b)) clearly reveal the aligning of individual ZnO nanoparticles in as flakes like top hills, strongly correlating the fact that successive deposition of the precursors are only allowed at the empty sites (such as the kinks, steps) on the preformed ZnO layers. Thus, it directed to grow individually along the preferred orientation, thereby maintained the integrity of the as-formed nanoparticulate films [35].

The presence of large lattice misfit between the deposited AGZO material and the Si substrate that occasionally hindered the growth of

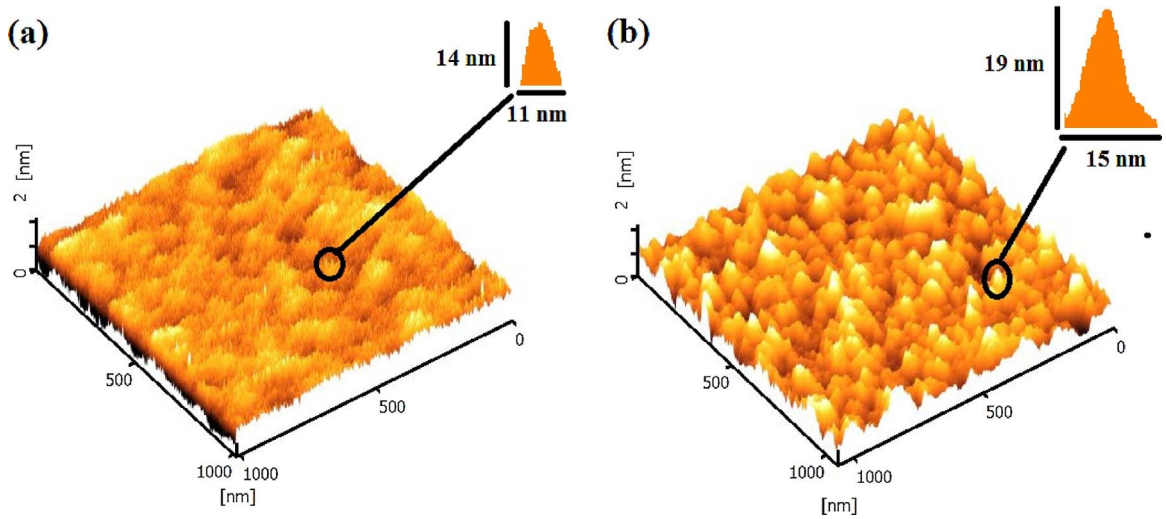

Fig. 4. 3D AFM images of different samples: (a) 1 h. (b) 3 h.

layers on the strained structure is manifested as film roughness. Consequently, the growth process is altered from layer-by-layer to spontaneous formation of three-dimensional Nano islands.

The baseline sample comprised of a distribution of pyramid-shaped grain that eventually transformed to dome-shaped upon annealing for 3 h. Furthermore, prolonged annealing caused these grains to coarsen via structural and compositional changes through continuous strain relaxation. Coarsening being a competitive growth processes, some islands are found to grow at the expense of others in order to minimize the total surface energy [36].This led to an enhancement in the mean volume of grains with annealing time. Coarsening in a system of pure ZnO clusters happens due to combined mechanisms such as Ostwald ripening [37] mediated by adatom diffusion between grains or Si inter-diffusion.

Table 3 enlists the values of increasing annealing time, roughness (rms), number density and ratio of grain area calculated from the AFM

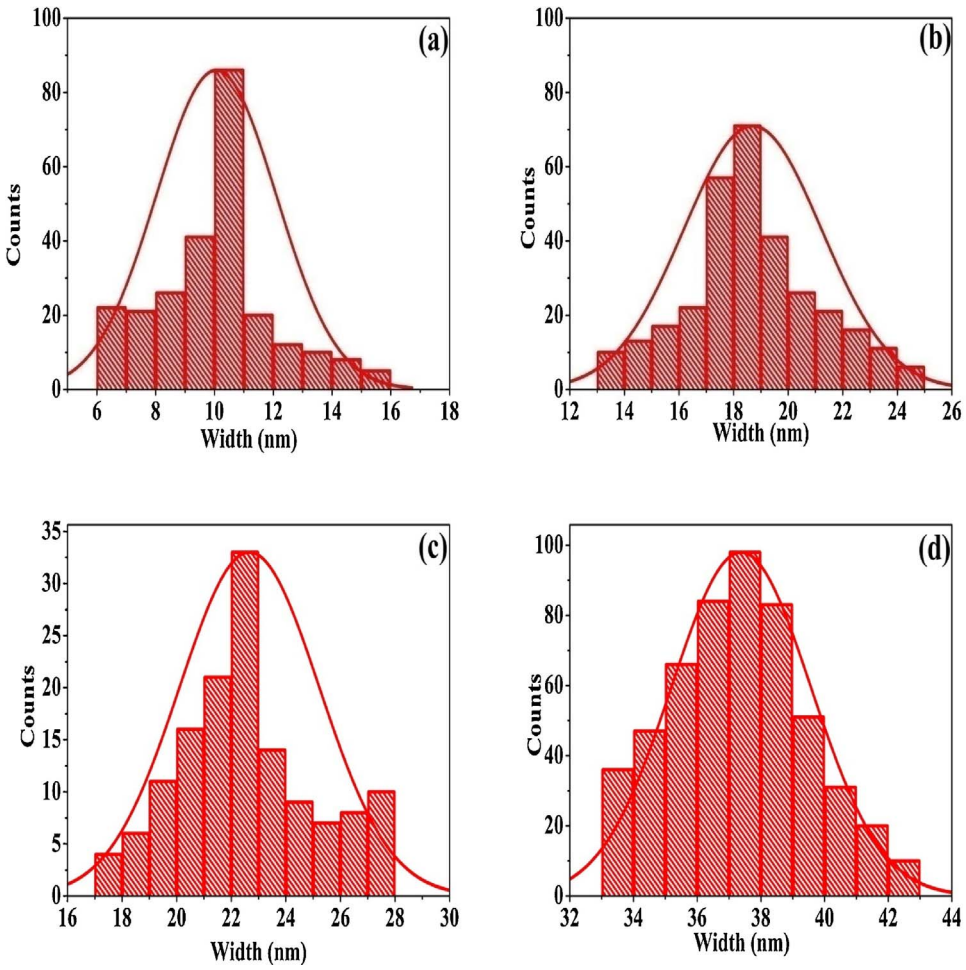

Fig. 5. Corresponding (Fig. 4) width distribution of grains in the samples: (a) as-prepared. annealed for (b) 1 h. (c) 2 h. (d) 3 h.

Table 3
Annealing time dependent NPs mean size, rms roughness, number density and ratio of grain area for synthesized AGZO nanofilm.

Annealing time (h)	RMS (nm)	Number density ($\times 10^{11}$ cm^{-2})	Ratio of grain area (%)	Average height (nm)	Average width (nm)
As prepared	3.172	0.2	28	10	12
1	5.692	0.8	38	11	14
2	8.054	1.2	46	13	16
3	10.183	1.4	62	15	19

data. The achieved enhancement in the values density and mean grain size with increasing annealing time is attributed to long range migration of atoms on the surface with longer free path, formation of more nucleation sites and subsequent growth processes. Moreover, the increase in the rms roughness is ascribed to the fluctuation of surface having different grains size distribution.

Fig. 6(a), (c), (e) and (g) demonstrate the FESEM images (planer view) of AGZO nanofilm including as-prepared and those synthesized for annealing time durations of 1, 2, and 3 h respectively. Except the as-prepared sample all others are comprised of mixed nanoparticales and nanoflakes morphology. Conversely, the non-annealed sample revealed homogenous surface containing a high density of grains lead to fewer nanoporous structures (black spots in Fig. 6(a)). However, the surface morphology of samples annealed at 1 h (Fig. 6(c)) and 2 h (Fig. 6(e)) is substantially different. This is because the annealing treatment has provided sufficient thermal energy for such nanostructures (NPs and nanoflakes) growth. The planer view of samples also depicted an overall increase in the NPs size consisting of little amount of large perpendicular nanoflakes (particles white in color in the Fig. 6e and g).

Further increase in the annealing time duration up to 3 h led to an enhanced crystallization of ZnO nanostructures, where the NPs size and number density both perpendicular and parallel to the nanoflakes are increased. The diameters of NPs are found to range from 10 to 36 nm. Some pieces of nanoflakes are entangled on the NPs (Fig. 6(b)). This increase in the grain size with the increase of annealing time also agreed with the XRD analysis. Such increase in the average diameter of the NPs with increasing annealing time is due to the Time extension by supplying the thermal energy agitated agglomeration of finer NPs. Moreover, the achievement of the improved morphology may be due to the reduction of no bridging oxygen defects and subsequent favorable formation of hexagonal structure [30].

According to the literature, the growth mechanism of ZNSs and their agglomeration in the absence of a seed layer or metal catalyst can be divided into two steps such as the nucleation and growth. Nucleation is defined as the agglomeration process of molecules to form the first grain of the nanostructure and the growth takes over when a critical nucleus is reached. In this process, the vapor of Zn powder reacts with the O_2 atoms during the heating process to form the nucleus of the ZnO. Then, the ZnO or Zn vapor condenses into liquid droplets of ZnO (l) or Zn (l) on the surface of the substrate [38]. Liquid droplets that are observed in the initial stage of the nanoflkes nucleation process create the favored nucleation sites on the substrate and subsequently the growth process begins from these sites[39].

Fig. 6(b), (d), (f) and (h) display the cross-sectional FESEM images of as-prepared, 1 h, 2 h, and 3 h annealed samples, respectively. The thickness uniformity over a large substrate area is confirmed through extensive inspection of the entire film cross-section (Fig. 6(b)). The thin film surface of as-prepared sample is completely devoid of any fragmented particles, where no perpendicular nanoflakes are seen in the absence of any annealing. However, the AGZO thin film with 1 h of annealing (Fig. 6(d)) clearly displayed the formation of dense nanoflakes with approximate length of 60 nm. Further increase in the annealing time duration (2 h) has remarkably enhanced the growth rate of nanoflakes (Fig. 6(f)). The cross-sectional morphology for the sample with 3 h of annealing (Fig. 6(h)) also demonstrated the growth of thick and dense grains. The observed growth of large crystallites with higher roughness indicates (micro flakes) and another low roughness indicates nanoflakes, the presence of some grains which are perpendicular to the substrate surface.

The mechanism for the formation of ZnO-embedded nanoflakes together with nanoparticles can be explained as follows. In the sol-gel assisted spin coating process, ZnAc upon reaction with $Al(NO_3)_3{\cdot}9H_2O$, $Ga(NO_3)_3{\cdot}9H_2O$, 2-propanol and ethanolamine produces AGZO nuclei. Due to the rotation and formation of irregular layers of unequal thickness (agglomerate of multi nanoparticles) these types of nanostuructures are generated. Furthermore, the complex reaction mechanism played a significant role on the morphology variation of AGZO nanostuructures. These AGZO NSs at the onset of saturation formed ZnO nuclei which is then grew up under controlled temperature at 500 °C, time, free energy of the precursors, and growth rate of the various facets of ZnO crystal resulted in such nanoflakes. Conversely, the oxidation at annealing time of 3 h resulted in the nanoflakes formation with gradually increased in the density. The positive stress of top oxide layer is believed to increase drastically at larger thickness, causing more deformations and enhanced nucleation rate. Increase in the annealing time caused an increase in the oxidation time, where the generated sufficient stress led to the formation of nanoflakes. The estimated grain sizes are 13, 23 and 30 nm for 1 h, 2 h and 3 h, respectively. Clearly, the estimated grain sizes are increased with increasing synthesis time. Thus, the growth time during the synthesis of ZnO by the sol-gel method played an important role on the overall morphology of ZNSs. Fig. 6(c) and (g) shows the surface morphologies of the ZnO powders prepared at various synthesis time ranging from 1 h to 3 h. The FESEM images of AGZO samples revealed agglomerated nanoflakes structures with high non-uniformity. At longer annealing time duration, the nanoflakes appeared thicker, bigger, with more in numbers as evidenced. In short, the increase in reaction time (annealing time) significantly affected the surface morphology.

The EDX spectra as showed in Fig. 7 for (sample (g) from Fig. 6) clearly exhibited the right elemental composition of the AGZO film in terms of elements including Zn, Si, O, Al, and Ga. The appearance of intense Zn peak indicates that these thin films are mainly composed of pure ZnO as supported by AFM and XRD results. Furthermore, the contents of Zn and O are found to decrease upon annealing, indicating that some of the Zn is vaporized, diffused inside the Si substrate and intermixed with Si.

Fig. 8 illustrates the room temperature PL spectra of all samples obtained at wavelength excitation (320 nm). The presence of intense UV peak in the range of 3.20 to 3.02 eV for four different AGZO samples certainly indicates their good quality and purity. Furthermore, the broadening of the peaks for the annealed samples clearly showed the increase in the grain size distribution. The observed red shift (~0.21 eV) of the PL peak for the 3 h annealed sample is attributed to increase in the grain size (PL peak shift towards lower energy because of de-confinement). The peak position revealed a blue shift at extended heating time duration, indicating a decrease in the band gap. This observation is ascribed to the quantum size effect [40]. Brus et al. [41] and Kayanuma et al. [42] also reported a decrease in the ZnO band gap with increasing crystalline size.

Upon prolonged annealing is majorly ascribed to the Si inter-diffusion related coarsening mechanism and subsequent reduction of the compressive stress. Since the photon-absorption and photo-excitation occurred inside the ZnO NPs thus the observed UV emission showed significant size dependence. The possibility of direct exciton radiative recombination responsible for the observed PL emission may not be ruled out [42]. In fact, during thin films growth, the oxygen deficient defects formed in the Si and ZnO matrix may have contributed to the emission process.

All AGZO thin films exhibited broad blue emission peaks.

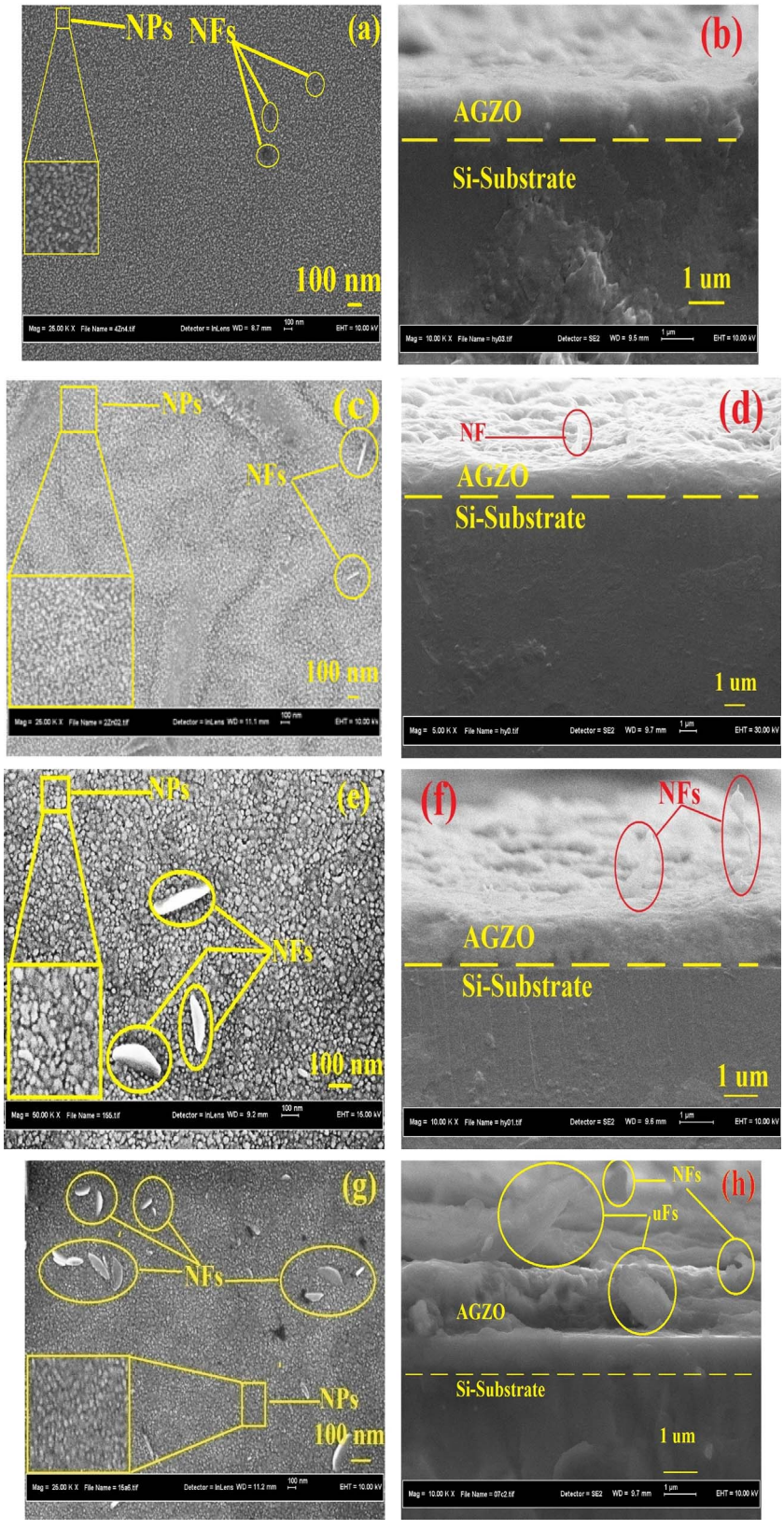

Fig. 6. FESEM images (top view) of AGZO nanofilms: (a) as-prepared and annealed for (c) 1 h. (e) 2 h. (g) 3 h. on the left. Inset shows the magnified view of selected area. The cross-sectional FESEM images of samples: (b) as-prepared and annealed for (d) 1 h. (f) 2 h. (h) 3 h.

Furthermore, the intensity of blue emission peak is found to enhance with the increase of NIR energy efficiency. It is worth noting that the blue emission depends on the relative concentrations of free electrons and defects created by oxygen vacancies in its lattice as a result of heating treatment [43]. This result is consistent with the XRD analysis, indicating that the crystal quality of the AGZO thin films can be controlled by adjusting the energy efficiency of the NIR process.

The occurrence of a broad size distribution of oxygen-passivated NPs in the film is responsible for the observed asymmetry and broadening of the PL peak. In addition, the near band-edge transition of the

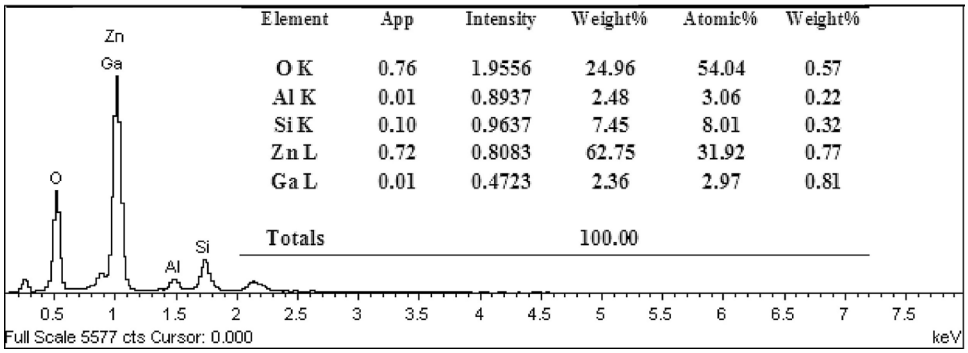

Fig. 7. Typical EDX spectra (for selected area) of AGZO nanofilms with 3 h annealing.

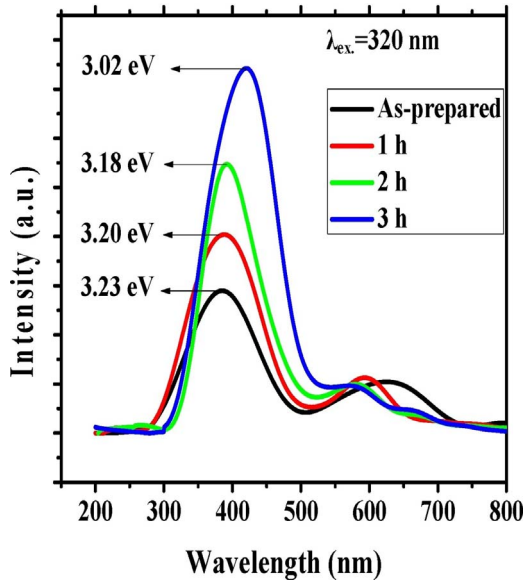

Fig. 8. PL spectra of synthesized AGZO samples as a function of annealing time.

wide band gap, especially the radiative recombination of the free excitons through an exciton–exciton collision process may contribute to the PL emission.

The electrical resistivity of as-prepared and annealed films is measured using four point probes method with silver as a contact electrode. The observed low conductivity of the as-grown films is attributed to the grain boundary effects as well as the adsorption of air (used as carrier gas). Furthermore, the possibility of chemisorptions of large number of oxygen molecules on the surface and grain boundaries of the film cannot be ruled out. This in turn created the potential barrier that affected the electrical transport, causing an enhanced electrical resistivity [44]. Annealing over prolonged duration may cause adesorption of oxygen ions from the samples, donating an electron to the atom. Thus, it reduced the resistivity by narrowing the grain boundary potential because the electrical conductivity depends on the number of charge carriers and their mobility [45]. The resistivity of the AGZO nanofilms (Table 2) is found to drop rapidly from 0.167 (as-prepared sample) to 0.024 Ω m (sample annealed for 3 h), indicating the attainment of a stable structure. Furthermore, the annealing mediated sufficient atomic diffusion may be responsible for the phase separation in the film [46]. This observation is consistent with the findings of Kim et al. [47].

Four-point probe is unable to detect the sheet resistance of as-deposited ZnO. This because many of the atoms are deposited at inappropriate positions before annealing and having low level of crystallinity as supported by the XRD analysis. However, annealing process has allowed the atoms to receive enough thermal energy for achieving equilibrium structure and subsequent reduction of the lattice strain. Thus, prolonged annealing allowed the formation of perfect crystalline structure, where the sheet resistance is reduced to a detectable range. The resistivity of synthesized thin films is calculated by multiplying sheet resistance. Table 2 enlisted the annealing time dependent resistivity of films and FWHM.

The observed decrease in the resistivity with increasing annealing time suggests that the atoms in the film received enough thermal energy to migrate to more suitable lattice sites for equilibration and thus formed more perfect crystals. The as-grown films displayed low conductivity, which may be due to grain boundary effects and adsorption of air that is used as carrier gas. There is a possibility of chemisorptions of large number of oxygen molecules on the surface and grain boundaries of the film, which can create the potential barrier that affects the electrical transport causing a reduction in conductivity [44].

The thin film is known to have lower resistivity as the structure is more crystalline with fewer defects, in other word the low for the first sample AGZO as grown with (FWHM = 0.01621) the resistivity was (0.167 Ω cm), When the annealing time became 3 h the crystallinity improved at low (FWHM = 0.0486) and the resistivity of this film decreased (0.024 Ω cm).

Fig. 9 displays the annealing time dependent Raman spectra of the prepared AGZO film. ZnO crystal being comprised of 4 atoms per primitive cell the point group is C6 v with 12 ° of freedom for vibrational modes (nine optical and three acoustic phonon modes). The Raman active optical modes at the C point include C optic = $A_1 + E_1 + 2E_2 + 2B_1$. $A_1(Z)$, $E_1(x)$, E1(y) and E_2, except the silent mode (B_1). The E_2 optical mode is observed at 101 cm^{-1} and 441 cm^{-1}. Modes such as $E_2(TO)$, $A_1(TO)$, and $E_1(TO)$ are evidenced at 334 cm^{-1}, 381 cm^{-1}, and 410 cm^{-1}, respectively. The higher order Raman peaks are evidenced at 547 cm^{-1}($2B_1$), 580 cm^{-1} (TA + TO), 661 cm^{-1}

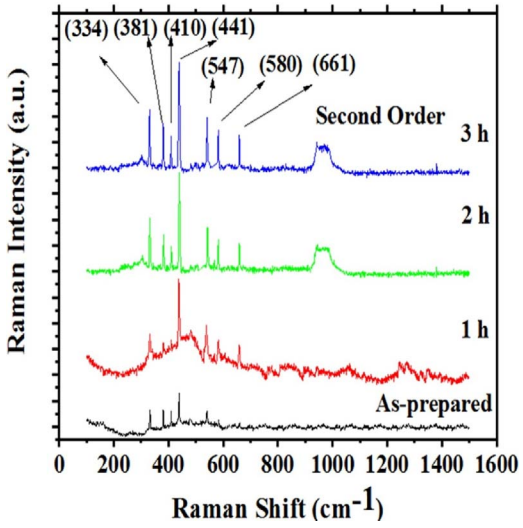

Fig. 9. Raman spectra of AGZO film: (a) as-prepared. and annealed at (b) 1 h. (c) 2 h. (d) 3 h.

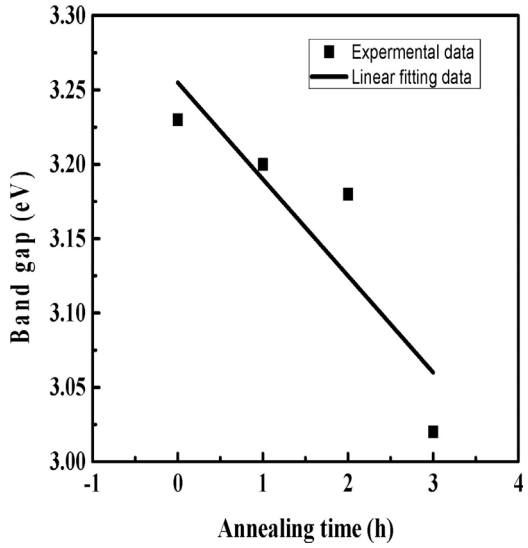

Fig. 10. Annealing time dependent variation in the band gap of AGZO nanostuructures films (filled squares are the experimental data and the solid line is the best fit).

(TA + LO), and 976 cm^{-1} (2LO). Our observation for the optical phonon modes are in good agreement with the findings of Irimpan et al. [48], Arguello et al. [49], Calleja and Cardona [50], and Serrano et al. [51]. The intensities of the Raman peaks for all samples are dropped with increasing annealing time, where the intensity and line shape of the second-order Raman peak around 976 cm^{-1} is most affected.

The samples annealed for 2 and 3 h revealed stronger intensity related to the Raman mode (441 cm^{-1}) than those of as-prepared and 1 h treated samples. The occurrence of sharp peak centred at 441 cm^{-1} is assigned to the normal lattice of ZnO crystals. With the increasing heating time (annealing), the intensity of the peak at 441 cm^{-1} is enhanced, confirming the improvement of crystallinity. This finding is consistent with that of the XRD measurement [52].

The reduction of the second-order Raman peak intensity for sample annealed at 3 h is strongly related to strong crystallinity because it is not affected much.

The narrowing of the band gap (E_g) in AGZO nanofilms with increasing annealing time can be understood using a mathematical formula that has been suggested and based on the line fitting data. The variation of E_g with annealing time obeys the relation [53]:

$$E_g = 3.255 - 0.065\ t \quad (6)$$

Where t is the annealing time for AGZO nanostructure films. This relation shows a negative gradient meaning that the value of E_g is decreased with increasing annealing time. The fitted data of band gap variation with the annealing time agreed well with the experimental data (Fig. 10). The rate of decrease in the value of E_g is linearly proportional to the annealing time duration.

4. Conclusion

Influences of annealing time on the structure, morphology and PL properties of AGZO nanofilms are examined. These films are deposited on Si substrate using sol-gel and spin coating methods and characterized via analytical measurements. AFM and FESEM images of synthesized samples revealed the existence of NPs and nanoflakes structures. XRD pattern confirmed the good crystallinity of samples and EDX spectra confirmed the appropriate elemental traces in the grown films. PL spectra showed the intense UV peak accompanied by a red shift in the peak intensity as well as broadening with increasing annealing time, which is attributed to the quantum confinement effect of photo carriers. Raman spectra exhibited various phonon modes, where the intensity of Raman peaks are greatly affected by the annealing treatment. Prolonged annealing duration (3 h) resulted lattice contraction and strain relaxation. Grain density, size, resistivity and occupancy are discerned to be strongly sensitive to the annealing time. It is demonstrated that by controlling the annealing time it is possible to tune the overall morphology, structure and optical properties on AGZO films prerequisite for diverse applications. Based on the results, we assert that the present moderate temperature growth mode of AGZO nanofilms is prospective for the development of good quality materials processing. The proposed material may be useful for the fabrication of biosensors, full-colour display, and integrated optoelectronics technology.

Acknowledgments

The authors are grateful to the Malaysian Government for providing the financial support through FRGS vote 4F815 in this project. Thanks also address to RMC and UTM for monitoring the research progress and fund managements and the performance of the project. Thanks are also extended to the Higher Education and Scientific Research, Al-Qadisiyah University, Faculty of Education, Physics Department of Iraq, for providing PhD study leave.

References

[1] D.V. Talapin, N. Gaponik, H. Borchert, A.L. Rogach, M. Haase, H. Weller, J. Phys. Chem. B 106 (2002) 12659–12663.
[2] Ü. Özgür, Y.I. Alivov, C. Liu, A. Teke, M. Reshchikov, S. Doğan, V. Avrutin, S.-J. Cho, H. Morkoc, J. Appl. Phys. 98 (2005) 041301.
[3] D.C. Look, Mater. Sci. Eng.: B 80 (2001) 383–387.
[4] S. Minne, S. Manalis, C. Quate, Appl. Phys. Lett. 67 (1995) 3918–3920.
[5] T. Chen, D. Ghosh, D. Krautz, S. Cheylan, V. Pruneri, Appl. Phys. Lett. 99 (2011) 093302.
[6] S. Salam, M. Islam, A. Akram, Thin Solid Films 529 (2013) 242–247.
[7] G. Rusu, M. Gîrtan, M. Rusu, Superlattices Microstruct. 42 (2007) 116–122.
[8] T. Ohgaki, N. Ohashi, H. Kakemoto, S. Wada, Y. Adachi, H. Haneda, T. Tsurumi, J. Appl. Phys. 93 (2003) 1961–1965.
[9] Y. Ryu, S. Zhu, J. Budai, H.R. Chandrasekhar, P.F. Miceli, H. White, J. Appl. Phys. 88 (2000) 201–204.
[10] B. Li, Y. Liu, Z. Chu, D. Shen, Y. Lu, J. Zhang, X. Fan, J. Appl. Phys. 91 (2002) 501–505.
[11] A. Samavati, H. Nur, A.F. Ismail, Z. Othaman, J. Alloys Compd. 671 (2016) 170–176.
[12] Z.N. Kayani, F. Nazir, S. Riaz, S. Naseem, Superlattices Microstruct. 82 (2015) 472–482.
[13] M. Thirumoorthi, J.T.J. Prakash, Superlattices Microstruct. 85 (2015) 237–247.
[14] I.Y. Bu, Superlattices Microstruct. 96 (2016) 59–66.
[15] J.C. Fan, K. Sreekanth, Z. Xie, S. Chang, K.V. Rao, Prog. Mater. Sci. 85 (2013) 874–985.
[16] T. Ivanova, A. Harizanova, T. Koutzarova, B. Vertruyen, Superlattices Microstruct. 85 (2015) 101–111.
[17] X. Shu-Wen, Phys. Procedia 25 (2012) 345–349.
[18] J. Cho, J. Nah, M.-S. Oh, J.-H. Song, K.-H. Yoon, H.-J. Jung, W.-K. Choi, Jpn. J. Appl. Phys. 40 (2001) 1040–1043.
[19] K. Ozaki, M. Gomi, Jpn. J. Appl. Phys. 41 (2002) 5614–5617.
[20] W. Lee, S. Shin, D.-R. Jung, J. Kim, C. Nahm, T. Moon, B. Park, Curr. Appl. Phys. 12 (2012) 628–631.
[21] R. Ebrahimifard, M.R. Golobostanfard, H. Abdizadeh, Appl. Surf. Sci. 290 (2014) 252–259.
[22] J. Lu, L. Zhu, Z. Ye, F. Zhuge, Y. Zeng, B. Zhao, D. Ma, Appl. Surf. Sci. 245 (2005) 109–113.
[23] T. Nagase, T. Ooie, J. Sakakibara, Thin Solid Films 357 (1999) 151–158.
[24] W.M. Tsang, F.L. Wong, M.K. Fung, J. Chang, C.S. Lee, S.T. Lee, Thin Solid Films 517 (2008) 891–895.
[25] M. Park, S.M. Han, Thin Solid Films 590 (2015) 307–310.
[26] J.H. Wakelin, H.S. Virgin, E. Crystal, J. Appl. Phys. 30 (1959) 1654–1662.
[27] W.D. CallisterJr. (Ed.), Materials Science and Engineering: An Introduction, fourth ed., John Wiley & Sons, Inc. copyright, New York, 1997.
[28] M. Gondal, Q. Drmosh, Z. Yamani, T. Saleh, Appl. Surf. Sci. 256 (2009) 298–304.
[29] N.S. Kumar, K.V. Bangera, G. Shivakumar, Appl. Nanosci. 4 (2014) 209–216.
[30] L. Cavalcante, M. Anicete-Santos, F. Pontes, I. Souza, L. Santos, I. Rosa, M. Santos, L. Santos-Júnior, E. Leite, E. Longo, J. Alloys Compd. 437 (2007) 269–273.
[31] D. Behera, B. Acharya, J. Lumin. 128 (2008) 1577–1586.
[32] S. Baruah, J. Dutta, Sci. Technol. Adv. Mater. 10 (2016) 1–18.
[33] A. Samavati, Z. Othaman, S. Ghoshal, M. Mustafa, Chin. Phys. B 2 (2015) 459–466.
[34] L. Xu, X. Li, Y. Chen, F. Xu, Appl. Surf. Sci. 257 (2011) 4031–4037.
[35] M. Dhingra, N. Singh, S. Shrivastava, P.S. Kumar, S. Annapoorni, Sens. Actuators A Phys. 190 (2013) 168–175.
[36] A. Samavati, M. Mustafa, Z. Othaman, S. Ghoshal, J. Nanomater. 2015 (2015) 101–121.
[37] R. Viswanatha, P.K. Santra, C. Dasgupta, D. Sarma, Phys. Rev. Lett. 98 (2007)

255501–255511.
[38] F.H. Alsultany, Z. Hassan, N.M. Ahmed, Superlattices Microstruct. 92 (2016) 68–79.
[39] H. Abdulgafour, F. Yam, Z. Hassan, K. Al-Heuseen, M. Jawad, J. Alloys Compd. 509 (2011) 5627–5630.
[40] Y. Cai, X. Li, P. Sun, B. Wang, F. Liu, P. Cheng, S. Du, G. Lu, Mater. Lett. 112 (2013) 36–38.
[41] L. Brus, J. Phys. Chem. 90 (1986) 2555–2560.
[42] T. Omata, K. Takahashi, S. Hashimoto, Y. Maeda, K. Nose, S. Otsuka-Yao-Matsuo, Meeting Abstracts, The Electrochemical Society., 2009.
[43] J.C. Johnson, H. Yan, P. Yang, R.J. Saykally, J. Phys. Chem. B 107 (2003) 8816–8828.
[44] B. Joseph, K. Gopchandran, P.K. Manoj, P. Koshy, V. Vaidyan, Bull. Mater. Sci. 22 (1999) 921–926.
[45] N. Bouhssira, S. Abed, E. Tomasella, J. Cellier, A. Mosbah, M. Aida, M. Jacquet, Appl. Surf. Sci. 252 (2006) 5594–5597.
[46] K.-K. Kim, S. Niki, J.-Y. Oh, J.-O. Song, T.-Y. Seong, S.-J. Park, S. Fujita, S.-W. Kim, 97 (2005) 4.
[47] J.-P. Kim, J.-S. Bae, T.-E. Hong, M.-S. Won, J.-H. Yoon, B.-S. Lee, H.-J. Lee, Thin Solid Films 518 (2010) 6179–6183.
[48] L. Irimpan, V. Nampoori, P. Radhakrishnan, A. Deepthy, B. Krishnan, J. Appl. Phys. 102 (2007) 7.
[49] C. Arguello, D.L. Rousseau, S.P.S. d. Porto, Phys. Rev. 181 (1969) 1351–1364.
[50] J. Calleja, M. Cardona, Phys. Rev. B 16 (1977) 3753.
[51] J. Serrano, A. Romero, F. Manjon, R. Lauck, M. Cardona, A. Rubio, Phys. Rev. B 69 (2004) 14.
[52] M. Fang, Z. Liu, Ceram. Int. 43 (2017) 6955–6962.
[53] V. Kumar, R. Singh, N. Singh, A. Kapoor, R. Mehra, L. Purohit, Mater. Res. Bull. 48 (2013) 362–366.